Optimizing energy growth as a tool for finding exact coherent structures

D. Olvera* and R. R. Kerswell†
School of Mathematics, Bristol University, Bristol BS8 1TW, United Kingdom
(Received 30 January 2017; published 16 August 2017)

We discuss how searching for finite-amplitude disturbances of a given energy that maximize their subsequent energy growth after a certain later time T can be used to probe the phase space around a reference state and ultimately to find other nearby solutions. The procedure relies on the fact that of all the initial disturbances on a constant-energy hypersphere, the optimization procedure will naturally select the one that lies closest to the stable manifold of a nearby solution in phase space if T is large enough. Then, when in its subsequent evolution the optimal disturbance transiently approaches the new solution, a flow state at this point can be used as an initial guess to converge the solution to machine precision. We illustrate this approach in plane Couette flow by rediscovering the spanwise-localized "snake" solutions of Schneider *et al.* [Phys. Rev. Lett. **104**, 104501 (2010)], probing phase space at very low Reynolds numbers (less than 127.7) where the constant-shear solution is believed to be the global attractor and examining how the edge between laminar and turbulent flow evolves when stable stratification eliminates the turbulence. We also show that the steady snake solution smoothly delocalizes as unstable stratification is gradually turned on until it connects (via an intermediary global three-dimensional solution) to two-dimensional Rayleigh-Bénard roll solutions.

DOI: 10.1103/PhysRevFluids.2.083902

I. INTRODUCTION

Optimization has proved a powerful tool to extract information from the Navier-Stokes equations. In the shear flow transition problem, optimizing over all possible infinitesimal disturbances to find the one that maximizes the subsequent energy growth after some pre-selected time T has proven invaluable in exposing the generic energy amplification mechanisms present. Called variously transient growth [1,2], nonmodal instability [3], or optimal perturbation theory [4] (see the reviews in [3,5] as well as [6]), the approach reveals key aspects of the linearized dynamics around the reference state that have helped to interpret finite-time flow phenomena and pick apart what causes a transition. The approach owes its popularity to its linearity, which means that there are multiple ways to extract the optimals and the mathematics in each case is well understood (see, e.g., [3,7–9]). The downside of the approach is that it can say nothing about finite-amplitude disturbances or, in other words, what can happen a finite distance away from the reference state in phase space [10,11].

Conceptually, the remedy to this is simple: Let competing disturbances seeking to maximize the energy growth after time T all have the same initial finite energy E_0 and use the fully nonlinear Navier-Stokes equations as a constraint [12–14]. This, however, doubles the number of parameters (E_0 joins T) over which the results must be interpreted *and* leads to a fully nonlinear, nonconvex optimization problem where much less is known about its possibly multiple solutions (local as well as global maxima) or how to find them. So far, the solution technique has necessarily been iterative and this has revealed a number of interesting new insights into the transition problem [12,14–22] (see the review in [13]). For example, one can ask what the smallest (most "dangerous") energy disturbance is that can trigger a transition by some time T, with the answer in the large-T limit

*do12542@bris.ac.uk
†R.R.Kerswell@bris.ac.uk

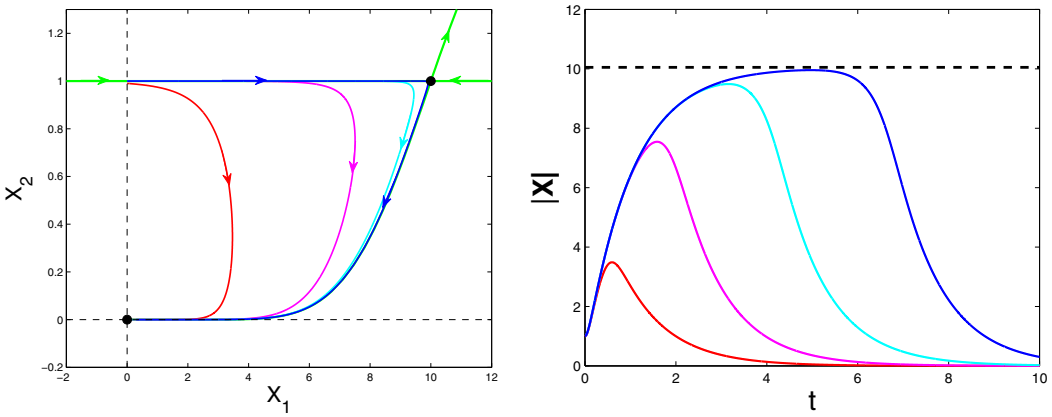

FIG. 1. Sample trajectories initiated close to the stable manifold ($X_2 = 1$) of the saddle point in the 2D model of [13]: $dX_1/dt = -X_1 + 10X_2$ and $dX_2/dt = X_2(10e^{-X_1^2/100} - X_2)(X_2 - 1)$ (left plot). The closer the initial conditions, the more a plateau in the norm $|\mathbf{X}|$ (here a proxy for the energy) where $\mathbf{X} := (X_1, X_2)$ develops near the value for the saddle point (marked as a dashed black line at $\sqrt{101}$) during the subsequent evolution (see the right plot). The initial conditions are $(X_1, X_2) = (0, 1 - \epsilon)$, where $\epsilon = 10^{-2}$ (red line), 10^{-5} (magenta line), 10^{-8} (cyan line), and 10^{-11} (blue line).

labeled the minimal seed for a transition [20–22]. The minimal seeds that emerge from this procedure are fully localized and are therefore realistic targets for experimental investigations (see, e.g., [21]).

The optimization approach works by naturally selecting disturbances on the energy hypersphere if they lie outside the basin of attraction of the reference state since then the energy remains finite for $T \to \infty$ (all other disturbances have to decay eventually). The new state to which these disturbances are drawn need not be a turbulent attractor and so the minimal disturbance to reach another simple stable state can also be calculated (see Sec. 6.2 in [23]). What is not so clear is whether the approach can find *unstable* solutions, although a similar line of reasoning seems to hold. The optimization procedure would be expected to select disturbances from the energy hypersphere that lie nearest or on the stable manifold of a nearby solution in phase space if T is large enough as this is the best way to avoid energy decay. The difference now, however, is since the nearby solution is unstable, T cannot be too large; otherwise even these disturbances will have decayed away (realistically, it is improbable to stay on the stable manifold to converge in to the unstable state). Once such an optimal disturbance has been found, its temporal evolution will show evidence of a transient approach to the alternative solution. Such an approach can be identified by noticing that the energy of the optimal disturbance plateaus near the energy of the different solution for some period of time. Figure 1 uses the simple two-dimensional (2D) model of [13] to illustrate this: The subsequent evolution of an initial condition taken closer and closer to the stable manifold of a nearby saddle point (actually the edge state in this model system) spends longer and longer close to the saddle before ultimately being repelled to the base state. A sufficiently close visit should yield flow states that can then be converged to the solution. The main purpose of this paper is to demonstrate that this approach can work.

We illustrate this in the context of plane Couette flow (PCF) by rediscovering the spanwise-localized "snake" solutions of Schneider *et al.* [24] building upon the prior exploratory work of Rabin (see Sec. 6.3 in [23]), who identified the key role played by the choice of E_0. In a wide geometry, snake solutions coexist with repeated copies of Nagata's well known solution [25] in a narrow geometry and, not surprisingly, the stable manifolds of the (lower-energy) snake solutions pass closer (in energy norm) to the constant-shear solution in phase space than those of Nagata's solution. However, the latter offer the possibility of greater energy growth as they lead to a global flow state and hence are preferred by the optimization algorithm if they pass close to the energy

hypersphere. As a result, Rabin found a threshold initial energy below which the optimal disturbance appears to approach a snake solution and above which Nagata's solution is approached (Sec. 6.3 [23]). We complete this calculation here by recomputing these optimal disturbances and converging both snake solutions.

Armed with this success, we then probe the phase space of PCF at very low Reynolds numbers (less than 127.7 [26]) looking for alternative solutions where the (basic) constant shear solution is believed to be the global attractor (a proof only exists for $\mathrm{Re} < 20.7$ [27]). We find evidence of solutions, but these turn out only to be the ghosts of known solutions at higher Reynolds numbers. Finally, as another example of how the optimization approach can be utilized, we examine how the edge between laminar and turbulent flow evolves when stable stratification suppresses the turbulence. With turbulence present, a bursting phenomenon sometimes forms a distinctive initial feature of the transition process for disturbances above the edge. This bursting is found to change little when the turbulent attractor vanishes under increasing stratification but disappears when a certain ECS ceases to exist. This then indicates that the bursting is directly related to the presence of the unstable manifold of this state directed away from the constant-shear solution in phase space.

The paper starts with the formulation of the stratified plane Couette flow problem in Sec. II A, which introduces the three nondimensional parameters that fully specify the problem once the computational box is chosen: the Reynolds number Re, the bulk Richardson number Ri_b, and the Prandtl number Pr with $\mathrm{Pr} = 1$ throughout. The optimization approach used and the iterative solution technique adopted are then described in Sec. II B. Section III is divided into three parts: A description of the wide domain computations to find the snake solutions is given first in Sec. III A, followed by a discussion of efforts to probe PCF at very low Re in Sec. III B, and then the calculations examining the bursting phenomenon are presented in Sec. III C. A final discussion in Sec. IV recaps the various results, provides some perspective, and then looks forward to future work.

II. FORMULATION

A. Stratified plane Couette flow

The usual plane Couette flow setup is considered in this paper of two (horizontal) parallel plates separated by a distance $2h$ with the top plate moving at $U\hat{\mathbf{x}}$ and the bottom plate moving at $-U\hat{\mathbf{x}}$. Stable stratification is added by imposing that the fluid density is $\rho_0 - \Delta_\rho$ at the top plate and $\rho_0 + \Delta_\rho$ at the bottom plate (gravity g is normal to the plates and directed downward from the top plate to the bottom plate). Using the Boussinesq approximation ($\Delta_\rho \ll \rho_0$), the governing equations can be nondimensionalized using U, h, and Δ_ρ to give

$$\frac{\partial \mathbf{u}}{\partial t} + \mathbf{u}\cdot\boldsymbol{\nabla}\mathbf{u} = -\boldsymbol{\nabla} p - \mathrm{Ri}_b \rho \hat{\mathbf{y}} + \frac{1}{\mathrm{Re}}\nabla^2\mathbf{u}, \tag{1}$$

$$\boldsymbol{\nabla}\cdot\mathbf{u} = 0, \tag{2}$$

$$\frac{\partial \rho}{\partial t} + \mathbf{u}\cdot\boldsymbol{\nabla}\rho = \frac{1}{\mathrm{Re}\,\mathrm{Pr}}\nabla^2\rho, \tag{3}$$

where the bulk Richardson number Ri_b, Reynolds number Re, and the Prandtl number Pr are respectively defined as

$$\mathrm{Ri}_b := \frac{\Delta_\rho g h}{\rho_0 U^2}, \quad \mathrm{Re} := \frac{Uh}{\nu}, \quad \mathrm{Pr} := \frac{\nu}{\kappa}. \tag{4}$$

Here $\mathbf{u} = (u, v, w)$ is the velocity field, κ is the thermal diffusivity, the total dimensional density is $\rho_0 + \rho\Delta_\rho$, p is the pressure, and ν is the kinematic viscosity. The boundary conditions are then

$$u(x, \pm 1, z, t) = \pm 1, \quad \rho(x, \pm 1, z, t) = \mp 1, \tag{5}$$

which admit the steady 1D solution

$$\mathbf{u} = y\hat{\mathbf{x}}, \quad \rho = -y. \tag{6}$$

The (possibly large) disturbance fields away from this basic state,

$$\tilde{\mathbf{u}}(x,y,z,t) = \mathbf{u} - y\hat{\mathbf{x}}, \quad \tilde{\rho}(x,y,z,t) = \rho + y, \tag{7}$$

conveniently satisfy homogeneous boundary conditions at $y = \pm 1$. Periodic boundary conditions are used in both the streamwise (x) and spanwise (z) directions over wavelengths $L_x h$ and $L_z h$, so the (nondimensionalized) computational domain is $L_x \times 2 \times L_z$. The total energy of the disturbance is taken as

$$E := \left\langle \tfrac{1}{2}\tilde{\mathbf{u}}^2 + \tfrac{1}{2}\mathrm{Ri}_b\tilde{\rho}^2 \right\rangle = \left\langle \tfrac{1}{2}(\mathbf{u} - y\hat{\mathbf{x}})^2 + \tfrac{1}{2}\mathrm{Ri}_b(\rho + y)^2 \right\rangle, \tag{8}$$

where $\langle(\cdot)\rangle := \frac{1}{V}\iiint(\cdot)dV$ is a volume average.

B. Methods

To find the largest energy growth that a (finite-amplitude) perturbation $(\tilde{\mathbf{u}},\tilde{\rho})$ can experience over a fixed time interval $[0,T]$ requires seeking the global maximum of the constrained Lagrangian

$$\begin{aligned}\mathcal{L} := &\left\langle \frac{1}{2}\tilde{\mathbf{u}}(\mathbf{x},T)^2 + \frac{1}{2}\mathrm{Ri}_b\tilde{\rho}(\mathbf{x},T)^2 \right\rangle + \lambda\left[\left\langle \frac{1}{2}\tilde{\mathbf{u}}(\mathbf{x},0)^2 + \frac{1}{2}\mathrm{Ri}_b\tilde{\rho}(\mathbf{x},0)^2 \right\rangle - E_0\right] + \int_0^T \langle \pi(\mathbf{x},t)\boldsymbol{\nabla}\cdot\tilde{\mathbf{u}}\rangle dt \\ &+ \int_0^T \left\langle \boldsymbol{\nu}(\mathbf{x},t)\cdot\left[\frac{\partial\tilde{\mathbf{u}}}{\partial t} + y\frac{\partial\tilde{\mathbf{u}}}{\partial x} + \tilde{v}\hat{\mathbf{x}} + \tilde{\mathbf{u}}\cdot\boldsymbol{\nabla}\tilde{\mathbf{u}} + \boldsymbol{\nabla}\tilde{p} + \mathrm{Ri}_b\tilde{\rho}\hat{\mathbf{y}} - \frac{1}{\mathrm{Re}}\nabla^2\tilde{\mathbf{u}}\right]\right\rangle dt \\ &+ \int_0^T \left\langle \tau(\mathbf{x},t)\cdot\left[\frac{\partial\tilde{\rho}}{\partial t} + y\frac{\partial\tilde{\rho}}{\partial x} - \tilde{v} + \tilde{\mathbf{u}}\cdot\boldsymbol{\nabla}\tilde{\rho} - \frac{1}{\mathrm{Re}\,\mathrm{Pr}}\nabla^2\tilde{\rho}\right]\right\rangle dt,\end{aligned} \tag{9}$$

where λ, π, $\boldsymbol{\nu}$, and τ are the Lagrange multiplier fields imposing the constraints that the initial perturbation energy is E_0, the perturbation is incompressible, and both the perturbation Navier-Stokes equation and the density equation are satisfied respectively. Taking variations with respect to all the degrees of freedom leads to the Euler-Lagrange equations that, beyond the aforementioned constraints, comprise the dual evolution equations for the fields $\boldsymbol{\nu} = \nu_1\hat{\mathbf{x}} + \nu_2\hat{\mathbf{y}} + \nu_3\mathbf{z}$ and τ,

$$\frac{\partial\boldsymbol{\nu}}{\partial t} + y\frac{\partial\boldsymbol{\nu}}{\partial x} - \nu_1\hat{\mathbf{y}} - \boldsymbol{\nu}\cdot(\boldsymbol{\nabla}\tilde{\mathbf{u}})^T + \tilde{\mathbf{u}}\cdot\boldsymbol{\nabla}\boldsymbol{\nu} + \boldsymbol{\nabla}\pi + \frac{1}{\mathrm{Re}}\nabla^2\boldsymbol{\nu} = \tau\boldsymbol{\nabla}\tilde{\rho} - \tau\hat{\mathbf{y}}, \tag{10}$$

$$\frac{\partial\tau}{\partial t} + y\frac{\partial\tau}{\partial x} + \tilde{\mathbf{u}}\cdot\boldsymbol{\nabla}\tau + \frac{1}{\mathrm{Re}\,\mathrm{Pr}}\nabla^2\tau = \mathrm{Ri}_b\nu_2, \tag{11}$$

the temporal end conditions

$$\tilde{\mathbf{u}}(\mathbf{x},T) + \boldsymbol{\nu}(\mathbf{x},T) = \mathbf{0}, \quad \mathrm{Ri}_b\tilde{\rho}(\mathbf{x},T) + \tau(\mathbf{x},T) = 0, \tag{12}$$

and the initial conditions

$$\frac{\delta\mathcal{L}}{\delta\tilde{\mathbf{u}}(\mathbf{x},0)} := \lambda\tilde{\mathbf{u}}(\mathbf{x},0) - \boldsymbol{\nu}(\mathbf{x},0) = \mathbf{0}, \quad \frac{\delta\mathcal{L}}{\delta\tilde{\rho}(\mathbf{x},0)} := \lambda\,\mathrm{Ri}_b\tilde{\rho}(\mathbf{x},0) - \tau(\mathbf{x},0) = 0. \tag{13}$$

To eliminate spatial boundary terms, $\boldsymbol{\nu}$ and τ are taken to obey the same homogeneous boundary conditions as $\tilde{\mathbf{u}}$ and $\tilde{\rho}$, and $\boldsymbol{\nu}$ is further assumed incompressible to automatically satisfy the Euler-Lagrange equation with respect to $\tilde{p}$. The solution strategy to find the global maximum of $\mathcal{L}$ is iterative, starting with a guess for the initial perturbation $(\tilde{\mathbf{u}},\tilde{\rho})$, which is then time stepped across the time interval $[0,T]$ via the Navier-Stokes equation. The final values of $\tilde{\mathbf{u}}$ and $\tilde{\rho}$ initiate $\boldsymbol{\nu}$ and τ [via conditions (12)] for the time integration of the dual equations (10) and (11) *backward* to $t = 0$ where the fact that Eqs. (13) are generally not satisfied is used to update the form of the initial

perturbation (subject to it staying of total energy E_0) in the direction of increasing $\mathcal{L}$. We use a simple steepest-ascent method

$$(\tilde{\mathbf{u}}^{(m+1)}(\mathbf{x},0),\tilde{\rho}^{(m+1)}(\mathbf{x},0)) = (\tilde{\mathbf{u}}^{(m)}(\mathbf{x},0),\tilde{\rho}^{(m)}(\mathbf{x},0)) + \frac{\epsilon}{\lambda}\left(\frac{\delta\mathcal{L}}{\delta\tilde{\mathbf{u}}(\mathbf{x},0)^{(m)}},\frac{1}{\mathrm{Ri}_b}\frac{\delta\mathcal{L}}{\delta\tilde{\rho}(\mathbf{x},0)^{(m)}}\right), \tag{14}$$

where, for example, $\tilde{\mathbf{u}}(\mathbf{x},t)^{(m)}$ is the mth iterate, ϵ is determined as in [20], and λ is subsequently chosen to ensure that the new $(m+1)$th iterate has energy E_0 as discussed in [13,14,20,22], but other approaches are possible (see, e.g., [12,15,17–19]). This direct and adjoint looping method is now well used (see, e.g., the reviews in [13,28]), but of course there is no guarantee that the global maximum always emerges for this fully nonlinear problem. The hoped output of the procedure is the optimal initial condition, the optimal disturbance, which experiences the largest growth over a time horizon $[0,T]$ of all initial conditions with the same initial total energy E_0 and so is a function of T and E_0.

The status of the iterative procedure is monitored by computing the residual

$$\mathcal{R}(m) := \frac{\langle|\delta\mathcal{L}/\delta\tilde{\mathbf{u}}(\mathbf{x},0)^{(m)}|^2\rangle + \frac{1}{\mathrm{Ri}_b}\langle|\delta\mathcal{L}/\delta\tilde{\rho}(\mathbf{x},0)^{(m)}|^2\rangle}{\langle|\boldsymbol{v}(\mathbf{x},0)^{(m)}|^2\rangle + \frac{1}{\mathrm{Ri}_b}\langle|\tau(\mathbf{x},0)^{(m)}|^2\rangle}, \tag{15}$$

which should approach 0 for convergence. The time integrations of the Boussinesq equations forward in time and the dual equations backward in time were carried out using an adapted version of the parallelized DNS code Diablo [29], which uses a third-order mixed Runge-Kutta-Wray–Crank-Nicolson time stepper. The horizontal directions are periodic and treated pseudospectrally (dealiased), while a second-order finite-difference discretization is used in the cross-stream direction. The resolution used was typically 64 Fourier modes per 2π in x and z and 128 finite-difference points in y. If needed, this resolution was doubled to ensure numerical accuracy. Diablo was coupled to a Newton-Raphson-GMRES algorithm [30], which allowed exact coherent structures (ECSs) to be converged from a good guess and continued around in parameter space (most notably by varying Ri_b). In what follows, it is usually more convenient to plot the gain $\mathcal{G}$ of iterates, which is defined as

$$\mathcal{G}(E_0,T) := \frac{E(T)}{E(0)}, \tag{16}$$

where $E_0 = E(0)$ is the *a priori* fixed initial perturbation energy; maximizing this, of course, is equivalent to maximizing the final total energy over all perturbations with given initial energy E_0.

III. RESULTS

A. Wide domain PCF: Rediscovering snakes

Optimal energy growth calculations were performed at $\mathrm{Re} = 180$ with stratification turned off ($\mathrm{Ri}_b = 0$) in the two wide domains $4\pi \times 2 \times 8\pi$ and $4\pi \times 2 \times 16\pi$ where the snake solutions are known to exist [24,31]. The calculations were initiated with random initial conditions (energy scattered in the lowest modes) normalized so that the total kinetic energy was E_0. If E_0 is too small, only the immediate neighborhood of the constant shear solution is explored with a nonlinear version of the 2D linear optimal, a global set of streamwise rolls [4], emerging as the optimal. If E_0 is too large, the optimal perturbation leads to another global state resembling multiple copies of Nagata's solution (see, e.g., Fig. 6.13 in [23]). Flows states from this optimal evolution could presumably be used to converge Nagata's solution, but this was not pursued (it would be more numerically efficient to treat a narrower domain that supports just one spanwise wavelength if that was an objective). At intermediary E_0, the optimal perturbation is more spanwise localized and stays spanwise localized as it evolves into a state suggestive of a snake solution (see Fig. 2).

Figure 2 (top left) shows the convergence features of the optimal growth calculation at this intermediary initial energy using $T = 150$ in the 16π wide box. The iterative algorithm is clearly struggling to converge—the residual remains $O(1)$—yet the gain has leveled off and most importantly

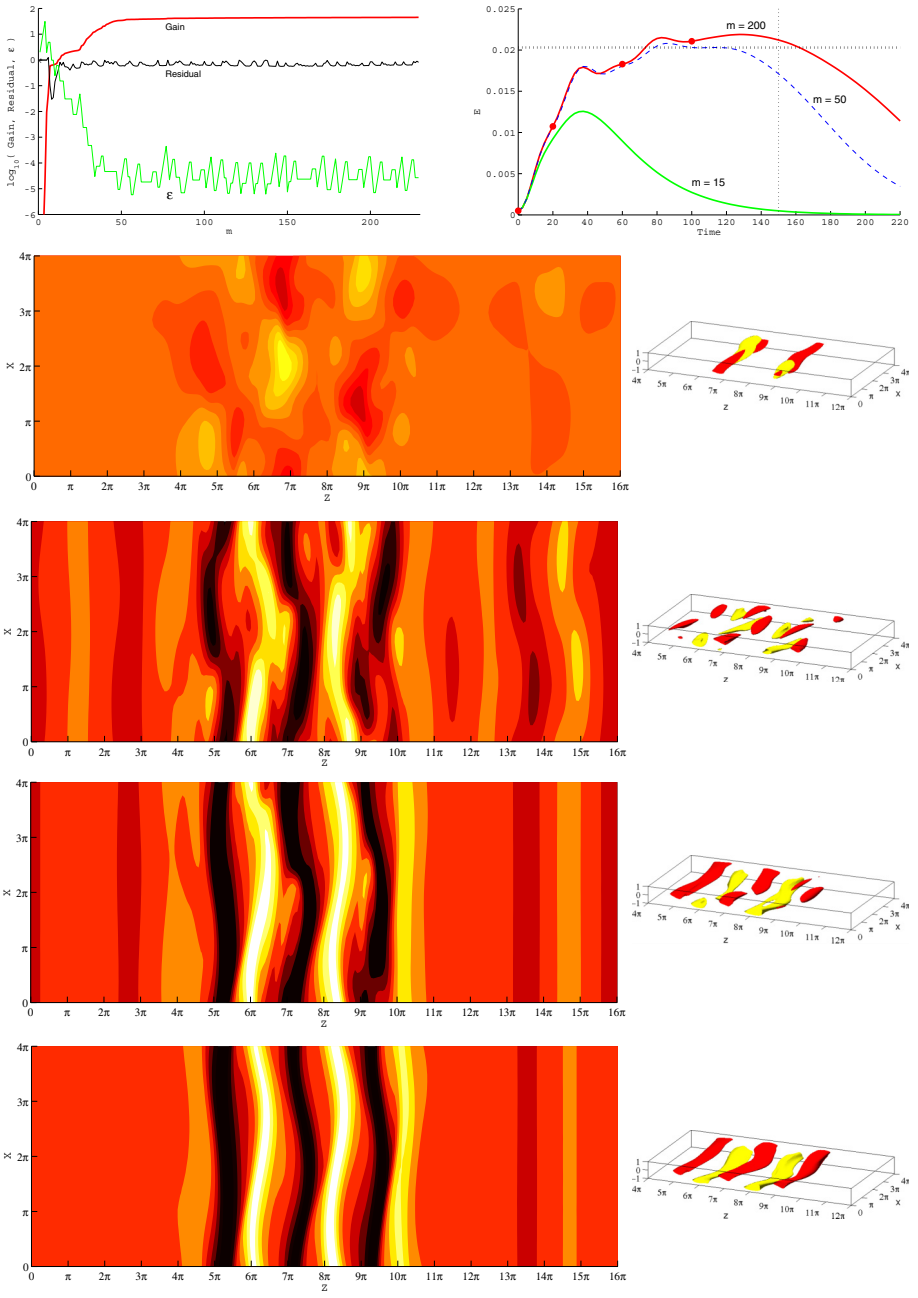

FIG. 2. The top left shows the gain (bold red line), residual (black line), and ϵ (green line) for variational computations with initial energy $E_0 = 5 \times 10^{-4}$ at $\mathrm{Re} = 180$, $\mathrm{Ri}_b = 0$, and $T = 150$ in a $4\pi \times 2 \times 16\pi$ domain [the computation is started with random noise, so the gain is $O(10^{-9})$ after one step of the algorithm]. The top right shows the time evolution of the initial perturbation for iterations $m = 15$, 50, and 200. The state at $t = 100$ from the initial condition at $m = 200$ is used as an initial guess for the Newton GMRES method. A horizontal dotted line shows the level of kinetic energy of the subsequently converged solution shown in Fig. 3. The red dots indicate the evolution of the perturbation shown below at times $t = 0$, 20, 60, and 100 (top to bottom). The left column shows the xz cross section at $y = 0$ using eight contour levels (between -0.58 and 0.059) and the right column isocontours showing $\pm 60\%$ of the maximum streamwise perturbation velocity.

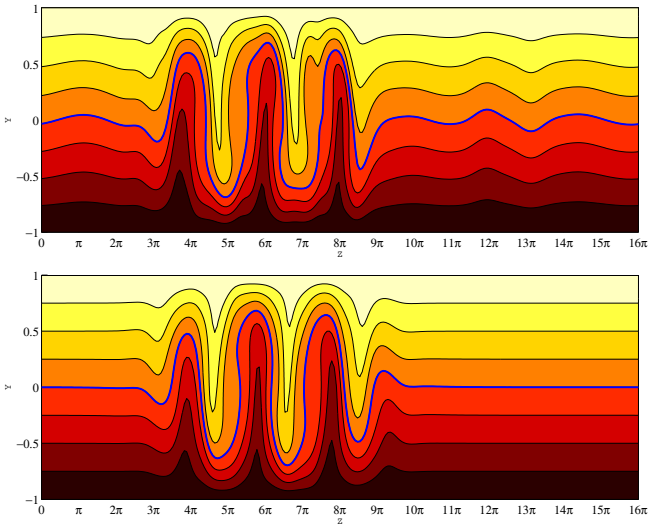

FIG. 3. Shown on top is the flow state used as an initial guess, the red circle marked at $t = 100$ in Fig. 2. Shown on the bottom is the converged state after 26 Newton steps. There are seven contour levels going from -1 to 1 with a blue isoline indicating $u = 0$.

a plateau has emerged in the time evolution of the optimal iterates (see the top right figure). This signals a close approach to a constant-energy saddle (either an equilibrium or traveling wave) and it is from here that we take a flow snapshot (specifically at $t = 100$) that is spanwise localized (see the top panel of Fig. 3). This state converged in 26 Newton steps to a very similar looking steady solution (see the bottom panel of Fig. 3), which is the equilibrium snake solution (EQ) of [31].

The optimization procedure proceeded much more slowly in the narrower domain $4\pi \times 2 \times 8\pi$ for reasons that are unclear, but again a plateau is eventually established in the optimal evolution (see the left plot of Fig. 4). Two flow states were extracted from this (top plots of Fig. 5) with one converging and one apparently not (see the bottom plots of Fig. 5) and the convergence behavior in

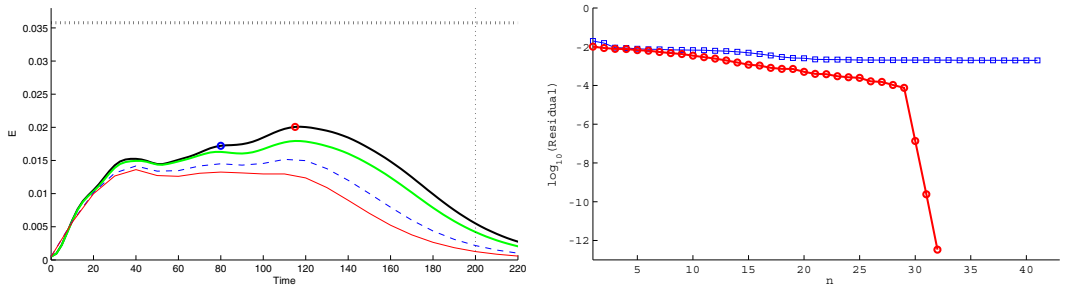

FIG. 4. Shown on the left is the time evolution of initial perturbations at various iterative stages ($m = 200$, red solid line; $m = 485$, blue dashed line; $m = 2280$, green solid line; and $m = 3000$, black solid line) in a domain $4\pi \times 2 \times 8\pi$ with $T = 200$. Dots on the $m = 3000$ iterate indicate states used as an initial guess for the Newton GMRES method. The horizontal dotted line shows the level of kinetic energy E of the solution converged from the $t = 115$ flow (bottom right, in Fig. 5). Shown on the right are the results of applying the Newton GMRES method to states taken at $t = 80$ and 115. Squares indicate the unsuccessful attempt starting from the state at $t = 80$, whereas the circles show successful convergence after 32 Newton steps starting with the state at $t = 115$.

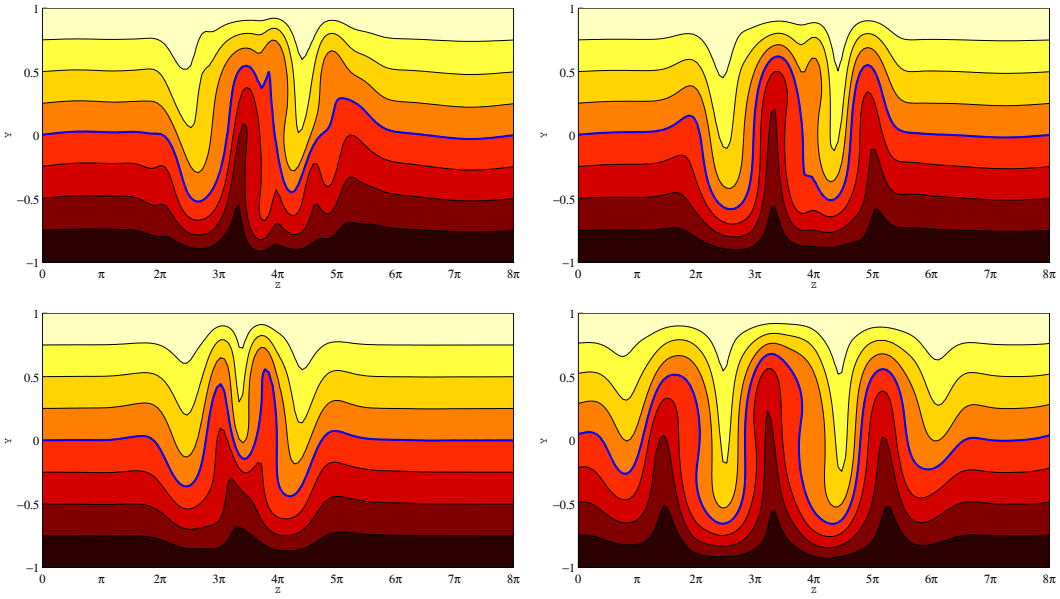

FIG. 5. The top left shows the state at $t = 80$ (blue circle in Fig. 4) with the unconverged result after $n = 41$ iterations in the bottom left. The top right shows the state at $t = 115$ (red circle in Fig. 4) and the converged solution achieved after $n = 32$ iterations in bottom right. The domain is $4\pi \times 2 \times 8\pi$ and there are seven contour levels going from -1 to 1 with a blue isoline indicating $u = 0$.

the right plot of Fig. 4. The converged state this time was the traveling-wave snake solution (TW) of [31].

Once the snake solutions EQ and TW had been found, they could be traced around in $(\mathrm{Re}, \mathrm{Ri}_b)$ parameter space ($\mathrm{Pr} = 1$ to keep things manageable) using the Newton GMRES algorithm. Fixing $\mathrm{Ri}_b = 0$ and varying Re in the 16π wide box reproduced the "snakes and ladders" plot of [24] (their Fig. 2) confirming the identity of the solutions (see the left plot of Fig. 6). Interestingly, setting

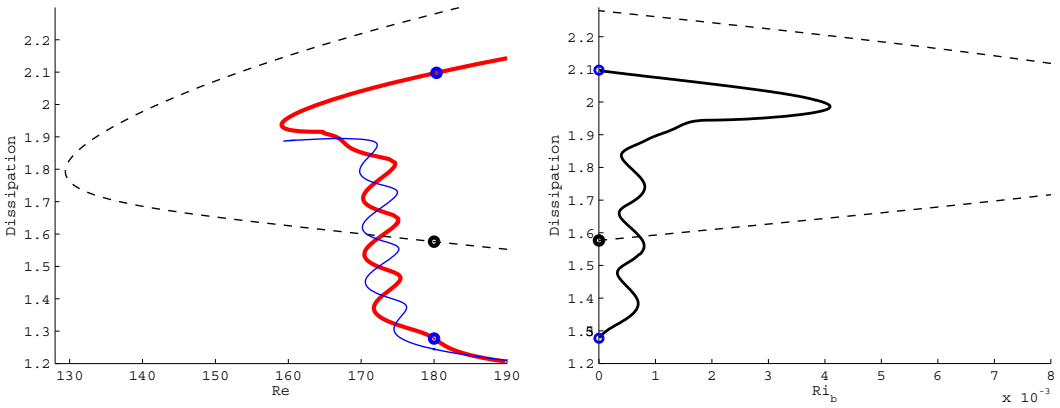

FIG. 6. Shown on the left is continuation in Reynolds number of the solutions converged in the domain $4\pi \times 2 \times 16\pi$ (the TW snake is the thin blue line and the EQ snake is the thick red line); compare with Fig. 2 from [24]. Circles indicates the states where continuation in Ri_b was started as shown in the right panel, which shows continuation in Ri_b at $\mathrm{Re} = 180$ for the Nagata solution (spanwise wave number $k = 1$) and the EQ snake.

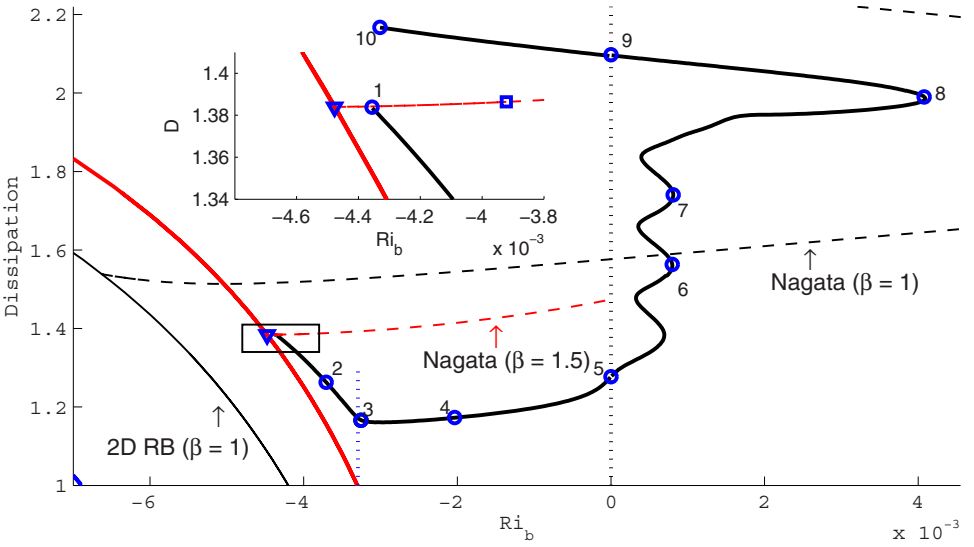

FIG. 7. Continuation in Ri_b of the equilibrium snake solution at fixed $\mathrm{Re} = 180$ extended to unstable stratification in the $4\pi \times 2 \times 16\pi$ box. The solution at each circle marked from 1 to 10 is visualized in Fig. 8. The inset shows the connection of the snake solution to the Nagata solution with spanwise wave number $\beta = 1.5$ (the black dashed line is the Nagata solution with spanwise wave number $\beta = 1$ shown in Fig. 6). The triangle marks the connection to the 2D convective rolls of Rayleigh-Bénard convection. The vertical blue dotted line marks the threshold of convective instability at $\mathrm{Ri}_b = -3.2943 \times 10^{-3}$.

$\mathrm{Re} = 180$ and varying Ri_b also shows snaking in EQ. Further continuing this solution to negative Ri_b (unstable stratification) (see Fig. 7) reveals that EQ connects to Nagata's solution (of different spanwise wave number $\beta = 1.5$ to that which the TW connects in Fig. 2 of [24] where $\beta = 1$). This connection is just after (as Ri_b increases) the Nagata solution bifurcates off a 2D convective roll solution familiar from the Rayleigh-Bénard problem (the extra shear from the boundaries does not affect this solution except to determine its orientation). Salewski *et al.* [32] have also recently found this same bifurcation sequence in rotating plane Couette flow, which is known to be closely related to the Rayleigh-Bénard problem.

In connecting to the $\beta = 1.5$ Nagata solution, the EQ snake solution has to delocalize and Fig. 8 shows this is a gradual process as Ri_b decreases from 0 as opposed to that found for Ri_b increasing from 0 when snaking occurs. The key observation for $\mathrm{Ri}_b < 0$ is that the (spatial) spanwise decay of the snake disappears once the threshold for convective instability at $\mathrm{Ri}_b = -3.2943 \times 10^{-3}$ is crossed [the critical Rayleigh number is defined as $-\mathrm{Ri}_b \mathrm{Re}^2 \mathrm{Pr} = 1708/16$; Salewski *et al.* [32] see the same phenomenon in rotating plane Couette flow (see their Fig. 4)]. This can be understood by examining the linear operator about the constant-shear basic state for the least-(spatially-)damped *temporally steady* eigenfunction since the deviation away from this constant-shear state becomes vanishingly small in the spanwise tails of the snake [33]. The snake becomes streamwise independent in its tail regions, suggesting analysis of the linear eigenvalue problem for 2D disturbances independent of the streamwise direction, i.e.,

$$(\tilde{\mathbf{u}}, \tilde{\rho}, \tilde{p}) = (\tilde{\mathbf{u}}(y), \tilde{\rho}(y), \tilde{p}(y)) e^{i\beta z + \sigma t}, \tag{17}$$

so that

$$\sigma \tilde{u} = \frac{1}{\mathrm{Re}} (\tilde{u}'' - \beta^2 \tilde{u}) - \tilde{v}, \tag{18}$$

$$\sigma \tilde{v} = \frac{1}{\mathrm{Re}} (\tilde{v}'' - \beta^2 \tilde{v}) - \tilde{p}' - \mathrm{Ri}_b \tilde{\rho}, \tag{19}$$

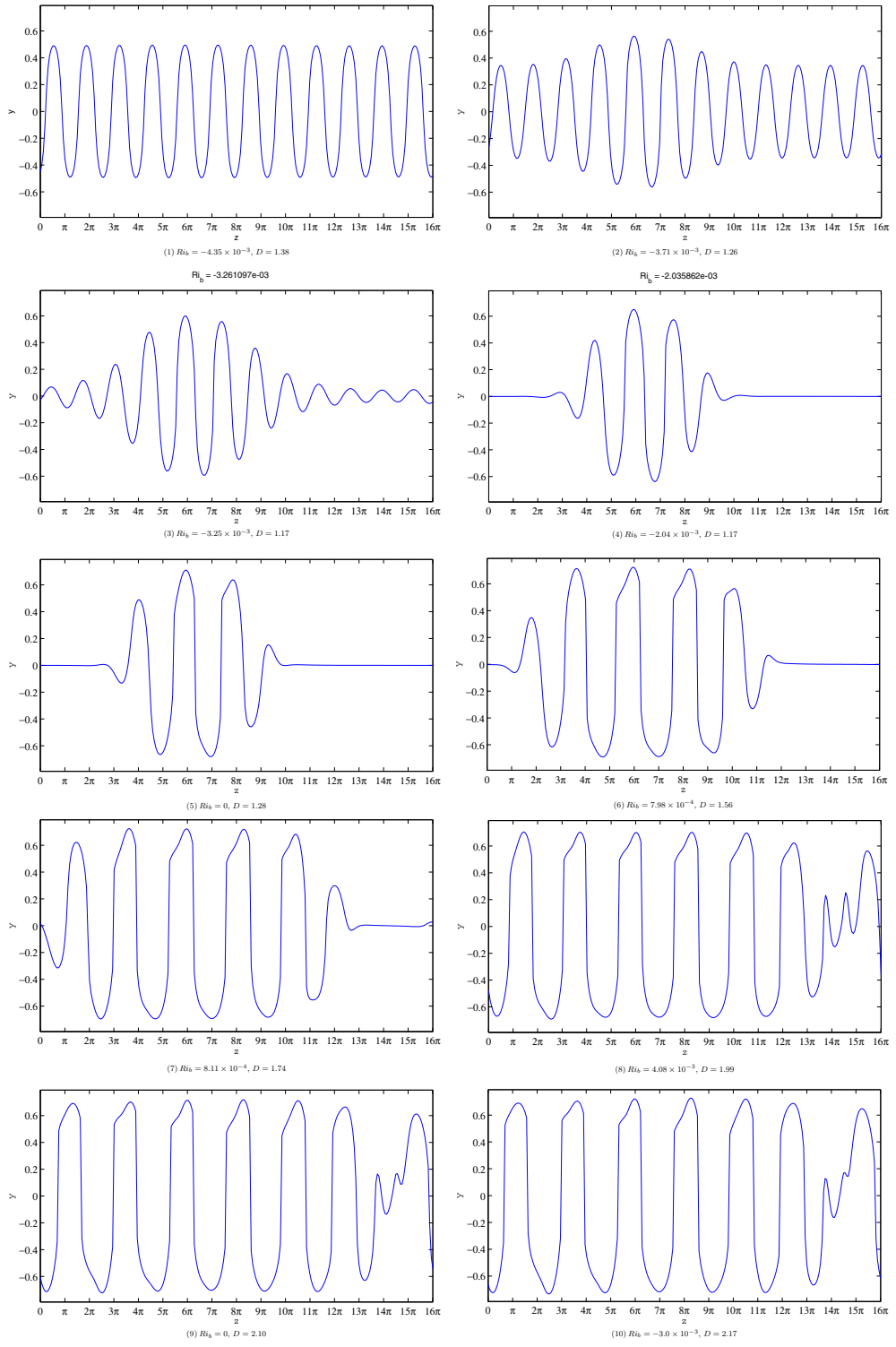

FIG. 8. Isolines for $u = 0$ of the streamwise component of the total flow of the equilibrium snake solution shown in Fig. 7. The labels refer to states at the numbered circles on the solution curve.

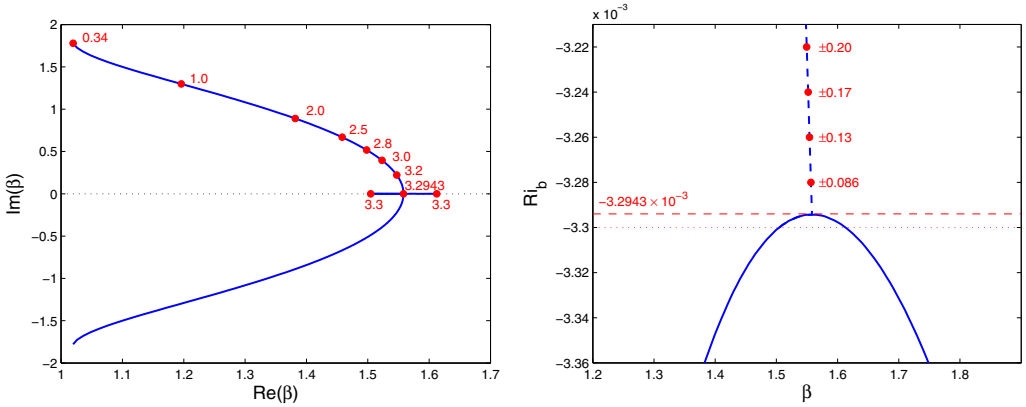

FIG. 9. Shown on the left is the complex wave number for steady 2D streamwise-independent disturbances as a function of Ri_b (labels are $-1000\,\mathrm{Ri}_b$) at $\mathrm{Re} = 180$. Here $\mathrm{Im}(\beta)$ indicates the spatial decay rate in the spanwise direction and $\mathrm{Re}(\beta)$ the spatial frequency. Neutral spatially periodic disturbances can exist for $\mathrm{Ri}_b \leqslant -3.2943 \times 10^{-3}$ (the Rayleigh-Bénard instability threshold) but have to become localized for larger (less negative) Ri_b indicated by $\mathrm{Im}(\beta) \neq 0$. Shown on the right is the neutral stability curve for Rayleigh-Bénard convection ($\mathrm{Ra} := -\mathrm{Ri}_b \mathrm{Re}^2 \mathrm{Pr}$) (see the Appendix). For $\mathrm{Ri}_b \leqslant -3.2943 \times 10^{-3}$ (solid blue line), temporally neutral disturbances exist for real wave numbers β, whereas for $\mathrm{Ri}_b > -3.2943 \times 10^{-3}$ (dashed blue line), the wave number has to be complex for temporal neutrality. In this case, the nonvanishing imaginary part is indicated in red at selected points along the dashed blue line. The left and right plots show the neutral curve in $(\mathrm{Re}(\beta), \mathrm{Im}(\beta), \mathrm{Ri}_b)$ space from two different perspectives.

$$\sigma \tilde{w} = \frac{1}{\mathrm{Re}}(\tilde{w}'' - \beta^2 \tilde{w}) - i\beta \tilde{p}, \tag{20}$$

$$0 = \tilde{v}' + i\beta \tilde{w}, \tag{21}$$

$$\sigma \tilde{\rho} = \frac{1}{\mathrm{Re}\,\mathrm{Pr}}(\tilde{\rho}'' - \beta^2 \tilde{\rho}) + \tilde{v}. \tag{22}$$

Normally, β is assumed real and the eigenvalue problem is scrutinized for complex σ with $\mathrm{Re}(\sigma) = 0$ to find spatially periodic eigenfunctions that are neither growing nor decaying in time. Here, instead, the interest is in (real) $\sigma = 0$ and complex β to find spatially decaying, temporally steady eigenfunctions (since EQ is steady). Of primary interest is the eigenfunction with the smallest amplitude of $\mathrm{Im}(\beta)$ since this has the slowest spatial decay in the spanwise direction. This behavior should dominate the spanwise evanescence of a steady ECS when the amplitude gets small (see Sec. 4.1 of [33]). Figure 9 shows this neutral curve in the complex β plane on the left and the usual neutral curve as viewed in the wave-number–control parameter plane is shown on the right. For $\mathrm{Ri}_b \leqslant -3.2943 \times 10^{-3}$, neutral spatially periodic eigenfunctions can exist, but otherwise $\mathrm{Im}(\beta) \neq 0$. Figure 10 shows that in the tail regions there is indeed a good correspondence between the expected spatial decay and the numerically observed decay close to the linear instability threshold at $\mathrm{Ri}_b = -3.2943 \times 10^{-3}$.

So, in summary, by using optimal energy growth, we have managed to rediscover the snake solutions of [24,31]. Having shown that this approach works, we now turn our attention to a region of parameter space in PCF where no solutions are currently known beyond the constant-shear base state.

B. Very low Re in PCF

In this section we turn stratification off ($\mathrm{Ri}_b = 0$) and set $\mathrm{Re} = 100$, which is above the energy stability threshold of 20.7 [27], up to which the constant-shear state is provably unique, and below

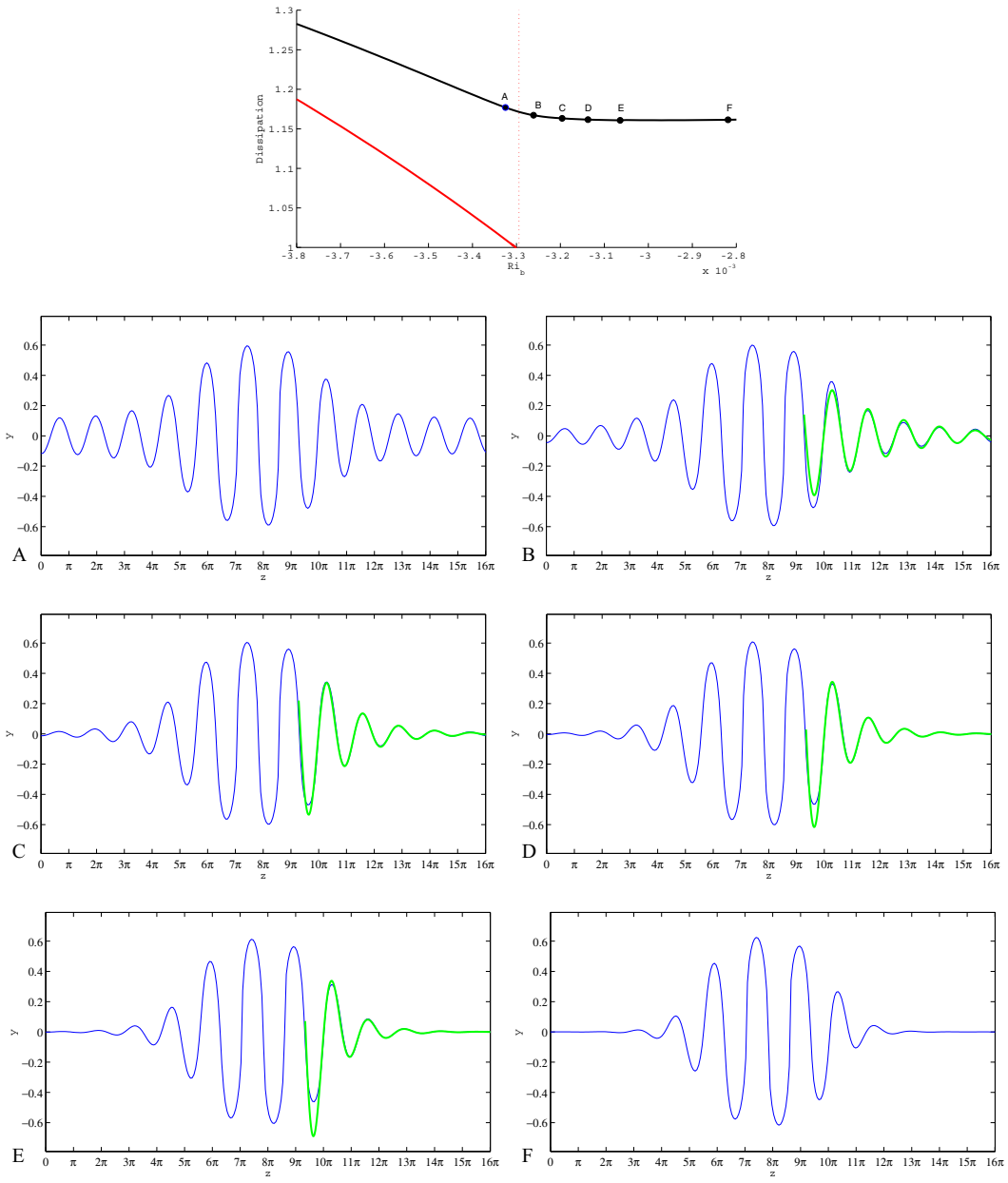

FIG. 10. Shown on top is a blowup of Fig. 7 centered on $\mathrm{Ri}_b = -3.2943 \times 10^{-3}$ (red dotted line). Note that there is a very small gap between where the roll solution (solid red line) bifurcates and the critical value of Ri_b (dotted red line) because the wave number that fits in a 16π wide box is slightly nonoptimal. The lower plots show isolines of $u = 0$ at $\mathrm{Ri}_b = -3.325 \times 10^{-3}$, curve A; $\mathrm{Ri}_b = -3.261 \times 10^{-3}$, curve B; $\mathrm{Ri}_b = -3.196 \times 10^{-3}$, curve C; $\mathrm{Ri}_b = -3.137 \times 10^{-3}$, curve D; $\mathrm{Ri}_b = -3.064 \times 10^{-3}$, curve E; and $\mathrm{Ri}_b = -2.819 \times 10^{-3}$, curve F, marked in blue with the predicted behavior at a large spanwise extent plotted in green.

127.7, which is the current best estimate of when other solutions start to exist [25,26]. A geometry of $4\pi \times 2 \times 2\pi$ and a rather short target time of $T = 20$ were chosen and E_0 gradually increased until the (nonlinear versions of the) first and second linear optimal perturbations (LOP_1 and LOP_2) shown in Fig. 11 were no longer found.

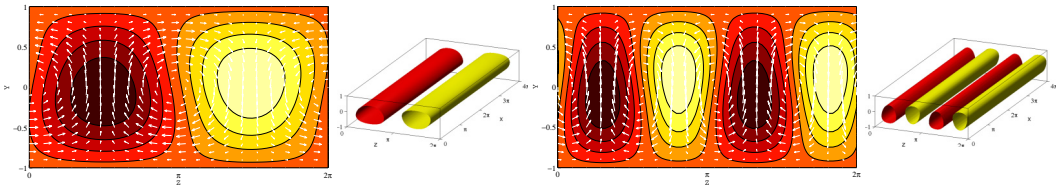

FIG. 11. LOP_1 (left) and LOP_2 (right) for $T = 20$ with $E_0 = 1.0 \times 10^{-4}$. Here LOP_1 is the 2D optimal shown in Fig. 4 of [4]. The same contour levels are used for both plots (eight levels between -0.004 and 0.004) and isocontours are $\pm 60\%$ of the maximum streamwise perturbation velocity.

At $E_0 = 10^{-3}$, a new nonlinear optimal perturbation ($NLOP_1$) emerges that actually experiences larger growth than both the LOP_1 and LOP_2 at earlier times. This initial condition is three dimensional, localized towards one wall, and evolves into two pairs of wavy fast-slow streaks (see Fig. 12). However, there is no discernible energy plateau in its evolution, so T was increased to 40, whereupon a different nonlinear optimal ($NLOP_2$) emerges at $E_0 \approx 1.5 \times 10^{-3}$; see Fig. 13 for its structure at $E_0 = 8 \times 10^{-3}$. This optimal gives rise to an energy plateau in its subsequent evolution as the initial energy is increased; see Fig. 14 for the situation at $E_0 = 8 \times 10^{-3}$. In this, a good candidate to initiate a convergence attempt is the flow state at $t = 16$, however, this simply converges to the constant-shear base state. Repeating the calculation at $\mathrm{Re} = 130$ (with $E_0 = 6 \times 10^{-3}$), again taking the flow state at $t = 16$, does converge but to Nagata's solution. A number of other searches were done for $\mathrm{Re} < 128$ with all guesses converging to the base state and for $\mathrm{Re} > 128$ where all attempts converged smoothly to Nagata's solution (the geometry is slightly suboptimal in that the saddle-node value for Nagata's solution is approximately equal to 128 rather than 127.7). No evidence emerged of any other state beyond Nagata's solution existing during these computations, adding further weight to the view that the constant-shear base state is a global attractor up to $\mathrm{Re} = 127.7$.

Despite this apparent simplicity, the results of a systematic optimal energy growth analysis over the (E_0, T) plane are still quite rich. Figure 15 indicates the various global optimals found at $\mathrm{Re} = 100$ and $T = 10$, 20, and 40 over the interval $E_0 \in [0, 0.01]$. At $T = 20$, for example, four different optimals emerge with all being the global optimal at some E_0 [see Fig. 15(b)]. That the nonlinear energy growth problem is nontrivial even in the absence of any exact coherent structures is presumably because phase space is already starting to structure itself to incorporate such states at slightly higher Re.

C. Stratified PCF for high Ri_b

As our third (and final) application of the optimal energy growth technique, we consider what happens to the edge, which in phase space separates states that become turbulent from those that

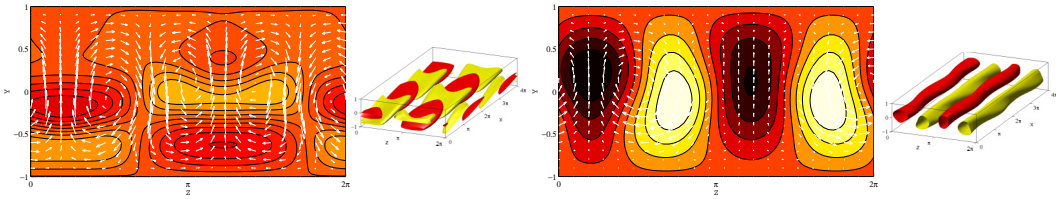

FIG. 12. Contours of streamwise velocity for $NLOP_1$ (left) using $T = 20$ at $E_0 = 1.0 \times 10^{-3}$ and what it evolves into at $t = 11$ (close to peak growth) on the right. The same contour levels are used for both plots (eight levels between -0.315 and 0.30) and the isocontours are $\pm 60\%$ of the maximum streamwise perturbation velocity.

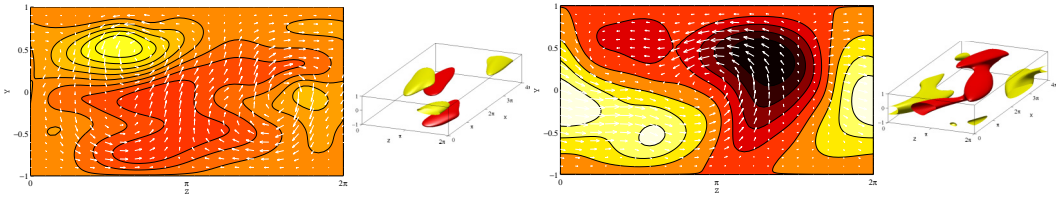

FIG. 13. Contours of streamwise velocity for NLOP$_2$ (left) using $T = 40$ at $E_0 = 8.0 \times 10^{-3}$ and what it evolves into at $t = 16$ (maximum kinetic energy) on the right. The same contour levels are used for both plots (eight levels between -0.72 and 0.58) and the isocontours are $\pm 60\%$ of the maximum streamwise perturbation velocity.

relaminarize, when the addition of stable stratification eliminates the turbulence. Direct numerical simulations [34] indicate that large energy growth can still occur and so we seek an explanation why by examining how the optimal energy growth perturbation changes as Ri_b increases from 0 in a geometry of $2\pi \times 2 \times \pi$ where $\mathrm{Re} = 400$.

There are two important values of Ri_b: the value $\mathrm{Ri}_b^t(\mathrm{Re})$ beyond which no turbulent attractor exists and the limiting value $\mathrm{Ri}_b^m(\mathrm{Re})$ for the existence of the global equilibrium EQ7 [35] [$10^{-6} < \mathrm{Ri}_b^t(400) \lesssim 10^{-2}$ and $\mathrm{Ri}_b^m(400) \approx 0.057$]. Here EQ7 is the edge state (the attracting state on the edge) for both $\mathrm{Re} = 800$ and $\mathrm{Re} = 1000$ with $\mathrm{Ri}_b = 0.001$ but *not* at $\mathrm{Re} = 400$ for either $\mathrm{Ri}_b = 0$ or $\mathrm{Ri}_b = 0.04$, where it has three unstable directions rather than the minimal one across the edge. Instead, Nagata's solution is the edge state until it disappears at $\mathrm{Ri}_b \approx 0.02$. Beyond this value, edge tracking is not possible as the turbulent state and the edge are not separated energetically. Previous work at $\mathrm{Re} = 1000$ by Rabin *et al.* [22] and Eaves and Caulfield [36] has identified the minimal seed for transition at $\mathrm{Ri}_b = 0$ and $0 < \mathrm{Ri}_b < \mathrm{Ri}_b^t$, respectively, which leads to EQ7 before leaving the edge for the turbulent attractor. Our focus here is $\mathrm{Ri}_b^t < \mathrm{Ri}_b$, but we start by looking at one value of $\mathrm{Ri}_b = 10^{-6} < \mathrm{Ri}_b^t$ to make contact with this earlier work.

Figure 16 shows partially converged optimal perturbations at $E_0 = 1.5 \times 10^{-4}$ using two target times $T = 50$ and 100, which both indicate that turbulence is triggered. Using $T = 50$, E_0 can be reduced until turbulence is no longer triggered by any iterate or the final converged optimal. At this point, $E_0 = E_c(50)$, the critical energy threshold for transition after a time $T = 50$ (suppressing

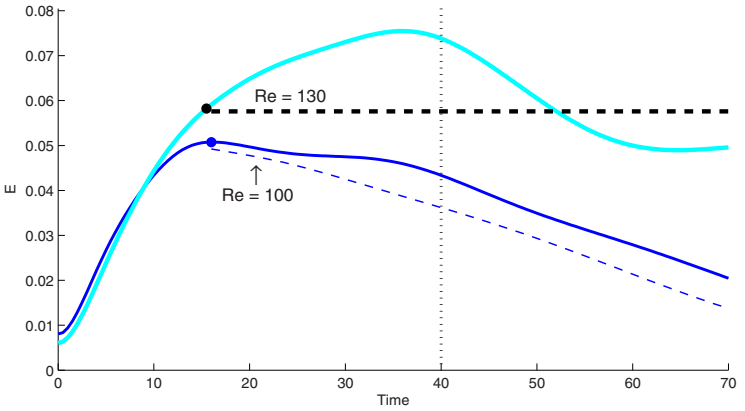

FIG. 14. Time evolution of optimal perturbations for $T = 40$. The blue line shows the evolution of NLOP$_2$ at $\mathrm{Ri}_b = 0$ for $\mathrm{Re} = 100$ at $E_0 = 8.0 \times 10^{-3}$ and the cyan line the evolution of NLOP$_2$ at $\mathrm{Ri}_b = 0$ for $\mathrm{Re} = 130$ at $E_0 = 6.0 \times 10^{-3}$. The circles indicate the states used as an initial guess for the GMRES algorithm and the dashed lines show the evolution of the GMRES output. When $\mathrm{Re} = 100$ at $E_0 = 8.0 \times 10^{-3}$ the GMRES iteration decays back to the laminar state. At $\mathrm{Re} = 130$, however, and $E_0 = 6.0 \times 10^{-3}$ the GMRES iteration converges to Nagata's solution.

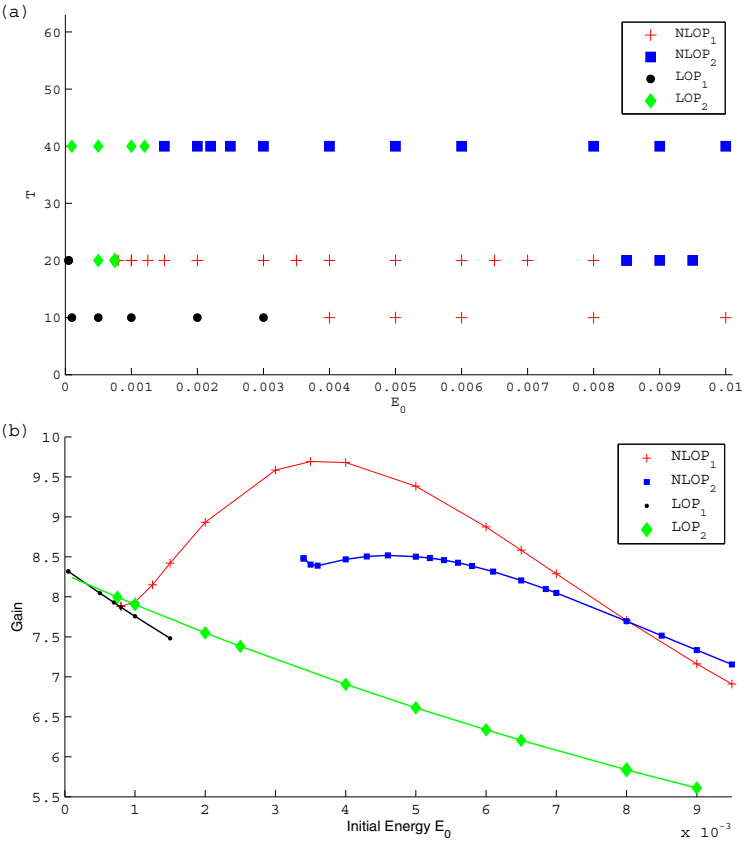

FIG. 15. Shown on the (a) is a plot of T against E_0 of optimal perturbations for Re $= 100$ in a $4\pi \times 2 \times 2\pi$ box indicating which type of optimal is the global optimal. On the (b) is a slice across the (a) plot at $T = 20$ showing optimal and suboptimal gains against initial energy E_0. Note that the preferred optimal quickly changes from LOP_1 (black line) to LOP_2 (green line) as E_0 increases from 0 and that NLOP_1 and then NLOP_2 eventually win out as global optimals.

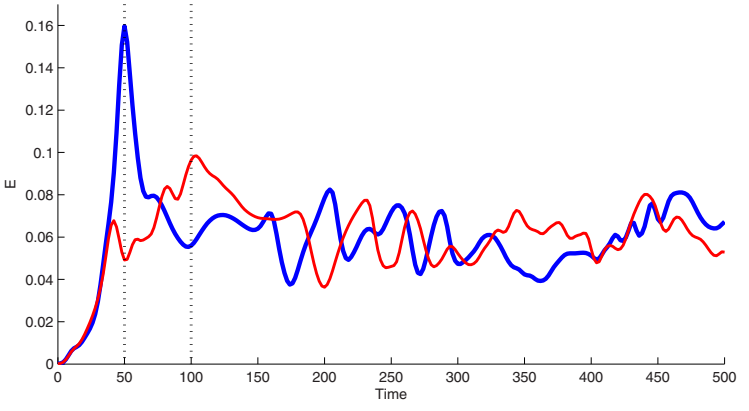

FIG. 16. Time evolution of initial conditions that lead to turbulence in very weakly stratified plane Couette flow at Re $= 400$ and $\mathrm{Ri}_b = 1.0 \times 10^{-6}$ in box size $2\pi \times 2 \times \pi$. The initial energy is $E_0 = 1.5 \times 10^4$ with the red line for target time $T = 100$ and the thicker blue line for $T = 50$.

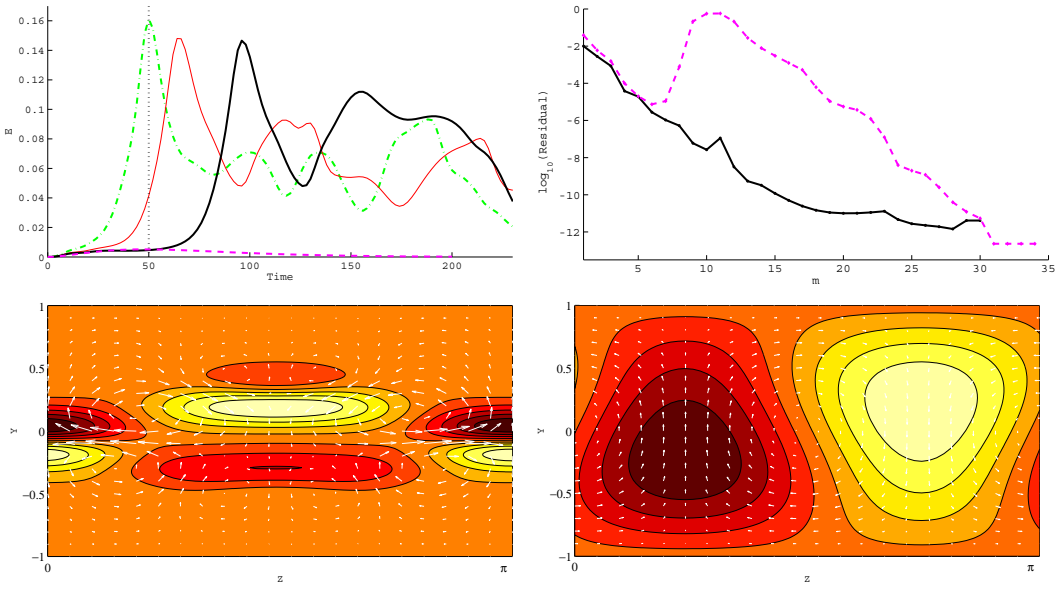

FIG. 17. The top left shows the time evolution of initial conditions at $\mathrm{Ri}_b = 1.0 \times 10^{-6}$, $\mathrm{Re} = 400$, and $T = 50$ for different initial energies: $E_0 = 9.0 \times 10^{-5}$ (green dash-dotted line), $E_0 = 6.0 \times 10^{-5}$ (red solid line), $E_0 = 5.0 \times 10^{-5}$ (black solid line), and $E_0 = 3.0 \times 10^{-5}$ (magenta dashed line). The critical energy E_c of the minimal seed lies between $E_0 = 3.0 \times 10^{-5}$ and $E_0 = 5.0 \times 10^{-5}$. The top right shows the residual as a function of iterate m for $E_0 = 5.0 \times 10^{-5}$ (solid black line) and $E_0 = 3.0 \times 10^{-5}$ (dashed magenta line). The bottom shows optimal perturbations (initial conditions) for $E_0 = 5.0 \times 10^{-5}$ (left) and $E_0 = 3.0 \times 10^{-5}$ (right) to maximize growth at $T = 50$ (the same eight contour levels are used for both plots).

dependence on Re and Ri_b for clarity), which is found to be between $E_0 = 3 \times 10^{-5}$ and 5×10^{-5} (see Fig. 17). The form of the optimal at 3×10^{-5} is still the nonlinearly adjusted LOP, whereas the optimal at 5×10^{-5} resembles the minimal seed found in [22] at $\mathrm{Ri}_b = 0$ (see Fig. 5 of [22]). The optimal for $E_0 = 5 \times 10^{-5}$ leads to an evolution from which a good enough starting guess can be extracted to converge EQ7 (not shown). This is another example where the approach has worked to identify an unstable state. In the original work of Rabin *et al.* [22] at $\mathrm{Re} = 1000$, EQ7 was an edge state and therefore could be approached using edge tracking, whereas here, at $\mathrm{Re} = 400$, EQ7 is not an attractor in the edge. Instead, it has been sought by the optimization procedure as trajectories that approach it experience the largest energy growth after $T = 50$.

Moving to stronger stratification, Fig. 18 shows converged optimals for $E_0 > E_c(50)$ with $\mathrm{Ri}_b = 0.01$ (which is just above Ri_b^t) and $\mathrm{Ri}_b = 0.04$. The former shows a transient turbulent episode while the latter only a burst of energy growth, which then decays away. Again, if E_0 is close enough to $E_c(50)$, the evolution of the optimal transiently visits the neighborhood of EQ7 sufficiently closely to be able to select a flow state that subsequently converges. For $\mathrm{Ri}_b = 0.04$, we find $2.102 \times 10^{-4} < E_c(50) < 2.108 \times 10^{-4}$ and a flow state taken at $t = 95$ from the $E_0 = 2.108 \times 10^{-4}$ optimal evolution converges in just seven steps to EQ7 (not shown).

Increasing the stratification further, Fig. 19 compares the results of working at $\mathrm{Ri}_b = 0.055 < \mathrm{Ri}_b^m$, where a burst is still discernible (notice the upward curvature of the energy curve), and $\mathrm{Ri}_b = 0.06 > \mathrm{Ri}_b^m$, where it is not. All indications (see, e.g., Figs. 18 and 19) are then that bursting is produced by the unstable manifold of EQ7 (directed away in phase space from the constant-shear basic state) and largely vanishes when EQ7 disappears (i.e., the upward curvature disappears). In fact, the phase space for $\mathrm{Ri}_b \gtrsim \mathrm{Ri}_b^m$ should still reflect the memory of the manifold, but this ebbs with increasing Ri_b. To confirm this simple explanation, we carried out a couple of checks. The

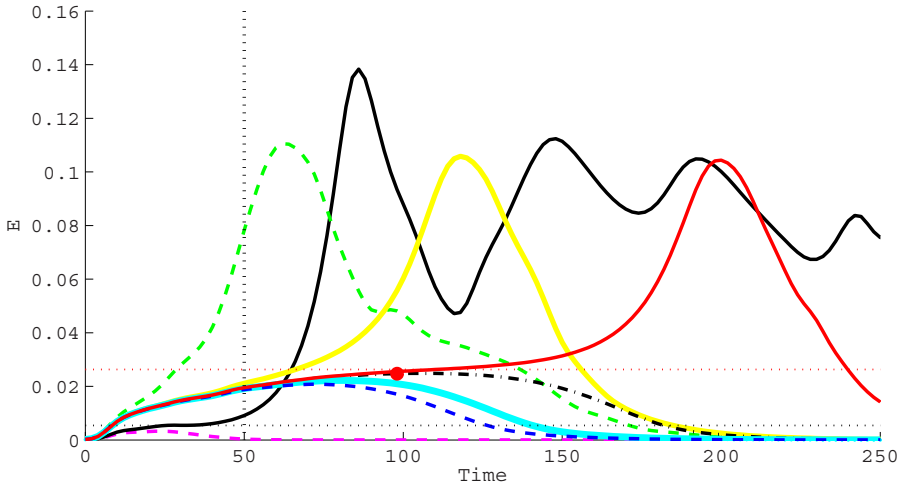

FIG. 18. Time evolution for optimal perturbations at Re = 400 and $T = 50$ in a box $2\pi \times 2 \times \pi$ for $\mathrm{Ri}_b = 0.01$ and 0.04. For $\mathrm{Ri}_b = 0.01$, E_c lies between $E_0 = 6.0 \times 10^{-4}$ (dashed magenta line) and $E_0 = 7.5 \times 10^{-4}$ (bold solid black line) with the lower horizontal black dotted line indicating the energy of EQ7 at $\mathrm{Ri}_b = 0.01$. A more detailed investigation at $\mathrm{Ri}_b = 0.04$ shows that E_c lies between $E_0 = 2.108 \times 10^{-4}$ (bold red line) and $E_0 = 2.102 \times 10^{-4}$ (dash-dotted black line). The state at $t = 95$ and $E_0 = 2.108 \times 10^{-4}$ (indicated by a red dot) can be converged in seven steps to EQ7, the energy of which is shown as the upper horizontal red dotted line.

first was to confirm that the state reached at the energy peak at pre- and post-Ri_b^m stratifications is roughly the same (see Fig. 20). The second was attempting to converge a flow state on an optimal energy plateau for $\mathrm{Ri}_b = 0.06$ [taken from the optimal evolution at $E_0 = 4.2 \times 10^{-4}$; see the red dot in Fig. 19(b)]. This failed to converge at Re = 400 but did converge to EQ7 at Re = 500 as $\mathrm{Ri}_b^m(400) < \mathrm{Ri}_b = 0.06 < \mathrm{Ri}_b^m(500)$ [see the inset of Fig. 19(b)].

The conclusion of this section is then that when the turbulence disappears, one still can see bursting because it is caused by the flow trajectory being repelled from the vicinity of the constant-shear base state by the unstable manifold of EQ7 normal to the edge. Since EQ7 is not the edge state, this bursting scenario is not generic for nearly marginal perturbations but nevertheless has been picked out by the optimization procedure; see [37] for a similar result in unstratified PCF. This bursting process survives well after the suppression of turbulence by stable stratification and relies only on EQ7 continuing to exist. To further confirm this picture, the optimal initial condition to trigger this bursting (as Ri_b increases) remains essentially the same across all Ri_b studied including $\mathrm{Ri}_b = 10^{-6}$, which is almost the unstratified case of [22] (see Fig. 21). However, what does change is the evolution of the optimal initial condition once it has experienced the burst in energy growth. Finally, we collect in Fig. 22 the data collected on E_c, the minimal energy to reach above the edge, as a function of Ri_b (the curve stops at $\mathrm{Ri}_b = 0.06$ since it is difficult to identify an edge beyond this point).

IV. DISCUSSION

In this paper we have demonstrated that an optimization technique, in which the energy growth of a finite-amplitude disturbance to a known solution is maximized, can be used to generate flow fields subsequently convergable via a Newton GMRES algorithm to another nearby solution of the Navier-Stokes equations. That this may be possible has been noticed before in the particular case of an edge state to which a flow initiated by the minimal seed will get infinitesimally close during its evolution [13,20,22]. Now this has been extended in Sec. III C to another ECS embedded in the edge that is *not* an attractor there. What was unclear before, however, was whether the technique

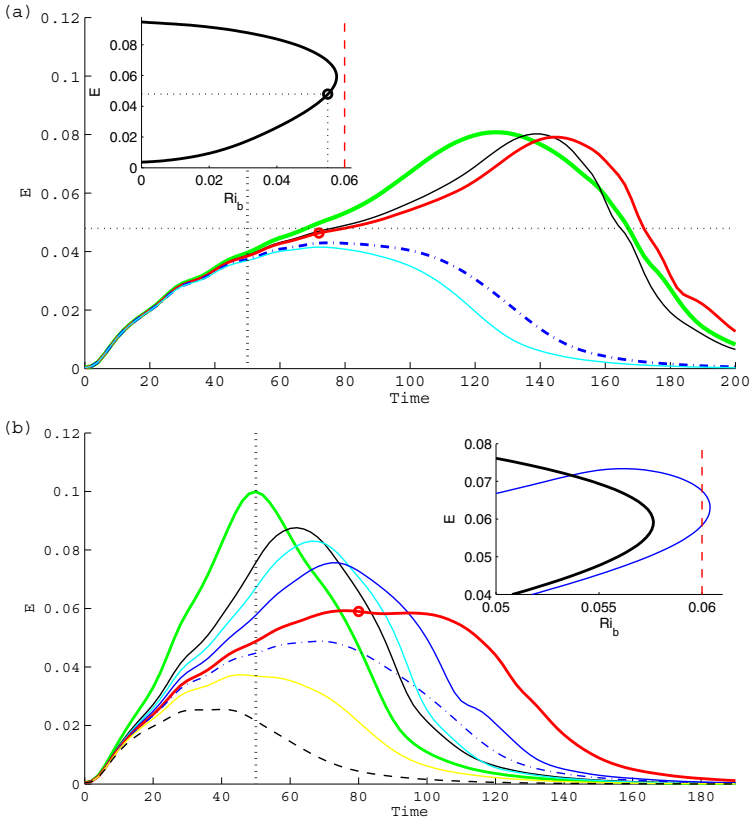

FIG. 19. Shown on the (a) is the time evolution for optimal perturbations at Re $= 400$ and $T = 50$ in a box $2\pi \times 2 \times \pi$ for $\mathrm{Ri}_b = 0.055$ for various E_0. Here E_c lies between $E_0 = 3.53 \times 10^{-4}$ (bold red solid line) and $E_0 = 3.525 \times 10^{-4}$ (dash-dotted blue line) with the lower horizontal black dotted line indicating the energy of EQ7 at $\mathrm{Ri}_b = 0.055$. Shown on the (b) is the time evolution of optimal perturbations for several E_0 in the same box for Ri $= 0.06$. No discernible critical E_0 can be detected as the magnitude of the burst decays monotonically. Here $E_0 = 5.0 \times 10^{-4}$, solid green line; $E_0 = 4.5 \times 10^{-4}$, solid black line; $E_0 = 4.4 \times 10^{-4}$, solid cyan line; $E_0 = 4.3 \times 10^{-4}$, solid blue line; $E_0 = 4.2 \times 10^{-4}$, bold red solid line; $E_0 = 4.15 \times 10^{-4}$, blue dash-dotted line; $E_0 = 4.05 \times 10^{-4}$, yellow solid line; and $E_0 = 3.80 \times 10^{-4}$, black dashed line. The flow state at $t = 80$ (red circle) from the $E_0 = 4.2 \times 10^{-4}$ trajectory was used as an initial guess for the Newton GMRES method but failed to converge. The inset shows the continuation in Ri_b at fixed Re $= 400$ (black bold line) and Re $= 500$ (blue line) of solution EQ7 making it clear that EQ7 does not exist at $\mathrm{Ri}_b = 0.06$ for Re $= 400$ but does at Re $= 500$.

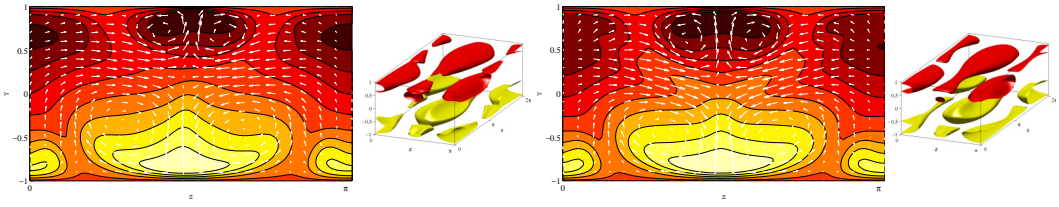

FIG. 20. Peaks of energy. The left plots show $\mathrm{Ri}_b = 0.04$ at $E_0 = 2.108 \times 10^{-4}$ and $t = 195$. The right plots show $\mathrm{Ri}_b = 0.06$ at $E_0 = 5.0 \times 10^{-4}$ and $t = 50$. The isocontours are $\pm 60\%$ of the maximum streamwise perturbation velocity and nine contour levels are used between -0.75 and 0.925.

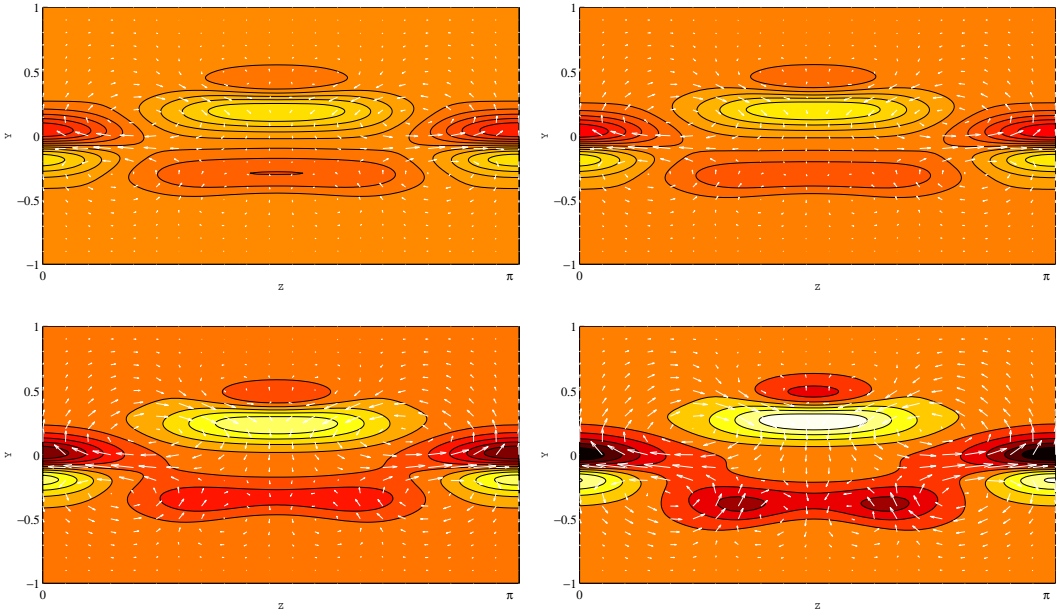

FIG. 21. Optimal perturbations. Contours of yz cross sections of streamwise perturbation velocity $\tilde{\mathbf{u}}(x,y,z,t)$ (arrows indicate velocity field in plane). The top left shows $\mathrm{Ri}_b = 1 \times 10^{-6}$ at $E_0 = 5.0 \times 10^{-5}$, the top right $\mathrm{Ri}_b = 0.01$ at $E_0 = 7.5 \times 10^{-5}$, the bottom left $\mathrm{Ri}_b = 0.04$ $E_0 = 2.104 \times 10^{-4}$, and the bottom right $\mathrm{Ri}_b = 0.06$ at $E_0 = 4.2 \times 10^{-4}$. The unstratified, weakly, and strongly stratified minimal seeds share the same structure. All plots use the same nine contour levels set by the extremes of the minimal seed at $\mathrm{Ri}_b = 0.6$ (arrows rescaled as well).

could be used to find unstable solutions more generally located in phase space in the absence of an edge. The rediscovery of both steady and traveling-wave snake solutions in Sec. III A demonstrates that the technique can also work in this situation too.

The technique was then used to probe very-low-Re PCF with negative results adding further weight to the view that the constant-shear solution is indeed the global attractor in PCF up to $\mathrm{Re} = 127.7$. It will be interesting to see if other techniques such as the steepest-descent approach recently developed in [38] similarly fail to find anything in this range. Finally, a bursting phenomenon was investigated in stably stratified PCF and found to be produced by the unstable manifold of an unstable ECS embedded in the edge: When this ECS vanishes on increasing the stratification so does the bursting. The key here is that the optimization technique allowed the bursting to be found and tracked as the stratification was varied even though the transition scenario is not the generic one mediated by the edge state.

Finally, the steady spanwise-localized snake solution was found to connect, via a global 3D state, to the 2D rolls of the Rayleigh-Bénard problem. In doing so, a particularly simple delocalization process was found where the spanwise tails of the snake gradually reduce their spatial decay rate until this vanishes at the global linear instability threshold whereupon the state is then global. This would seem a very generic phenomenon where a localized state moves from a region of subcriticality to one of supercriticality or vice versa.

The energy of the flow was selected as the functional to maximize in this work as this is the most logical historically (nonmodal analysis focuses on this; see, e.g., [3]), natural mathematically, and illustrates the phenomenology most clearly. However, there is no reason why other choices such as energy dissipation rate cannot be used. Then the concept of distance in phase space from the reference state changes of course, as will the attribute of what solutions are then closest to the

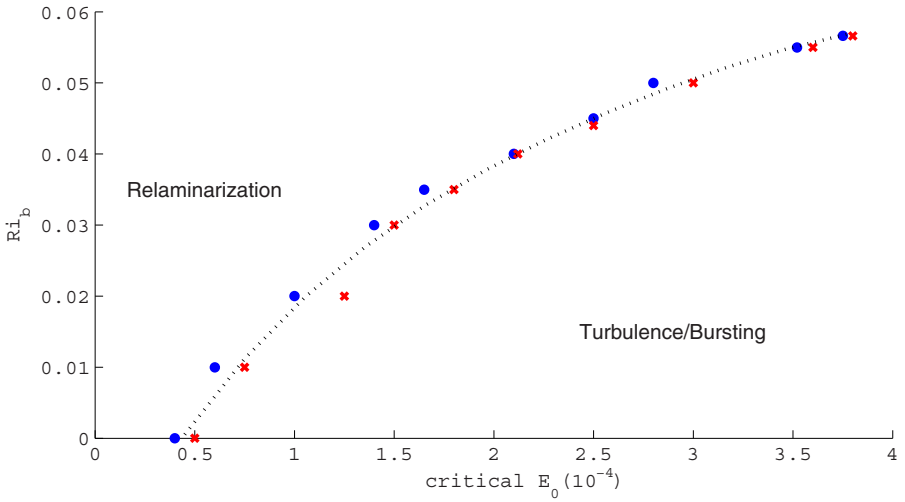

FIG. 22. Estimation of the curve of E_c for $\mathrm{Re} = 400$ and $T = 50$ in box $2\pi \times 2 \times \pi$. Turbulent events are marked as red crosses and relaminarization as solid blue dots. No discernible energy threshold is observed at $\mathrm{Ri}_b = 0.06$ when EQ7 no longer exists.

reference state. The key is that the functional is minimal at the reference state and so the optimization procedure will always seek optimals away from this.

In terms of further work, the most obvious question is whether the optimization technique can be used to find periodic orbits in which the energy varies in time. So far, only constant energy solutions (equilibria and traveling waves) have been sought and the identification of an energy plateau during the optimal's evolution has been central to indicate a close approach. In principle, a mildly fluctuating plateau should also be recognizable and provided the period is not too long, convergence should still be feasible. Another issue is whether the approach can provide any insight into phase space around a linearly *unstable* solution. Here the answer surely depends on the time scale τ of the linear instability. Typically the growth rates of linear instabilities in shear flows are much smaller than the typical instantaneous growth rates of energy growth optimals [e.g., in plane Poiseuille flow, the transient energy growth is at least an order of magnitude more than that from the linear instability over $O(100)$ advective times]. This then suggests that the optimization technique will simply ignore the linear instability for $T \ll \tau$ in preference to more potent mechanisms that give better, albeit transient, energy growth. One such mechanism could be a nearby stable manifold of another solution as explored here.

As a final comment, it is worth emphasizing that the principles that make the optimization approach work here in a fluid mechanical context hold true also for any dynamical system where solution multiplicity is suspected. What makes shear flows so interesting, of course, is this is now understood to be the generic situation where not only are there multiple solutions, but these are typically unstable yet instrumental in determining the fluid dynamics of the flow (e.g., the bursting of Sec. III C). This optimization approach then looks to be a valuable addition to a theoretician's toolbox.

ACKNOWLEDGMENTS

D.O. is grateful for a CONACYT scholarship and the availability of free HPC time on the University of Bristol's BlueCrystal supercomputer. Both D.O. and R.R.K. would like to thank Tom Eaves for sharing his nonlinear optimal perturbation routine (here converted to one focused on total energy rather than total dissipation), John Taylor for sharing his time-stepping code DIABLO, and

Dan Lucas for help parallelizing the GMRES algorithm used. We also are grateful to the rest of the EPSRC-funded (Grant No. EP/K034529/1) MUST team at Cambridge received during the course of this work.

APPENDIX: RAYLEIGH-BÉNARD CONVECTION

In the normal Rayleigh-Bénard setup [see, e.g., [39], Eqs. (8.6)–(8.8), with nonlinearities reinstated] the fully nonlinear equations for the total flow field $\mathbf{U}$ and temperature field Θ are

$$\frac{\partial \mathbf{U}}{\partial \tau} + \mathbf{U}\cdot\boldsymbol{\nabla}\mathbf{U} = -\boldsymbol{\nabla} P + \mathrm{Ra}\,\mathrm{Pr}\Theta\hat{y} + \mathrm{Pr}\nabla^2\mathbf{U}, \tag{A1}$$

$$\frac{\partial \Theta}{\partial \tau} + \mathbf{U}\cdot\boldsymbol{\nabla}\Theta = \nabla^2\Theta, \tag{A2}$$

$$\boldsymbol{\nabla}\cdot\mathbf{U} = 0, \tag{A3}$$

subject to boundary conditions

$$u(x,\pm 1,z,t) = \pm 1, \quad \theta(x,\pm 1,z,t) = \mp 1. \tag{A4}$$

Stratified plane Couette flow [as described by Eqs. (1)–(3)] is retrieved under the transformation

$$t = (\mathrm{Re}\,\mathrm{Pr})\tau, \quad \mathbf{u} = \mathbf{U}/(\mathrm{Re}\,\mathrm{Pr}), \quad \rho = \Theta, \quad p = P/(\mathrm{Re}\,\mathrm{Pr})^2 \tag{A5}$$

so that $\mathrm{Ra} = -\mathrm{Ri}_b\mathrm{Re}^2\mathrm{Pr}$. The critical Ra for linear instability is $\mathrm{Ra}_{crit} := 1708/16$, which is unchanged by introducing a unidirectional shear (see, e.g., [40]) (the factor of $1/16$ is because the half-channel width has been used to nondimensionalize the system).

[1] D. S. Henningson and S. C. Reddy, On the role of linear mechanisms in transition to turbulence, Phys. Fluids **6**, 1396 (1994).

[2] D. S. Henningson and S. C. Reddy, Energy growth in viscous channel flows, J. Fluid Mech. **252**, 209 (1993).

[3] P. J. Schmid, Nonmodal stability theory, Annu. Rev. Fluid Mech. **39**, 129 (2007).

[4] K. M. Butler and B. F. Farrell, Three-dimensional optimal perturbations in viscous shear flow, Phys. Fluids **4**, 1637 (1992).

[5] S. Grossmann, The onset of shear flow turbulence, Rev. Mod. Phys. **72**, 603 (2000).

[6] P. J. Schmid and D. S. Henningson, *Stability and Transition in Shear Flows* (Springer, New York, 2001).

[7] P. J. Schmid and L. Brandt, Analysis of fluid systems: Stability, receptivity, sensitivity, Appl. Mech. Rev. **66**, 024803 (2014).

[8] L. N. Trefethen, A. E. Trefethen, S. C. Reddy, and T. A. Driscoll, Hydrodynamic instability without eigenvalues, Science **261**, 578 (1993).

[9] L. N. Trefethen and M. Embree, *Spectra and Pseudospectra* (Princeton University Press, Princeton, 2005).

[10] O. Dauchot and P. Manneville, Local versus global concepts in hydrodynamic stability theory, J. Phys. (France) II **7**, 371 (1997).

[11] F. Waleffe, Transition in shear flows: Nonlinear normality versus non-normal linearity, Phys. Fluids. **7**, 3060 (1995).

[12] S. Cherubini, P. De Palma, J.-C. Robinet, and A. Bottaro, Rapid path to transition via nonlinear localized optimal perturbations in a boundary layer flow, Phys. Rev. E **82**, 066302 (2010).

[13] R. R. Kerswell, C. C. T. Pringle, and A. P. Willis, An optimisation approach for analysing nonlinear stability with transition to turbulence in fluids as an exemplar, Rep. Prog. Phys. **77**, 085901 (2014).

[14] C. C. T. Pringle and R. R. Kerswell, Using Nonlinear Transient Growth to Construct the Minimal Seed for Shear Flow Turbulence, Phys. Rev. Lett. **105**, 154502 (2010).

[15] S. Cherubini, P. De Palma, J.-C. Robinet, and A. Bottaro, The minimal seed of turbulent transition in the boundary layer, J. Fluid Mech. **689**, 221 (2011).

[16] S. Cherubini, P. De Palma, J.-C. Robinet, and A. Bottaro, A purely nonlinear route to transition approaching the edge of chaos in a boundary layer, Fluid Dyn. Res. **44**, 031404 (2012).
[17] S. Cherubini, J.-C. Robinet, and P. De Palma, Nonlinear control of unsteady finite-amplitude perturbations in the Blasius boundary-layer flow, J. Fluid Mech. **737**, 440 (2013).
[18] Y. Duguet, A. Monokrousos, L. Brandt, and D. S. Henningson, Minimal transition thresholds in plane Couette flow, Phys. Fluids **25**, 084103 (2013).
[19] A. Monokrousos, A. Bottaro, L. Brandt, A. Di Vita, and D. S. Henningson, Nonequilibrium Thermodynamics and the Optimal Path to Turbulence in Shear Flows, Phys. Rev. Lett. **106**, 134502 (2011).
[20] C. C. T. Pringle, A. P. Willis, and R. R. Kerswell, Minimal seeds for shear flow turbulence: Using nonlinear transient growth to touch the edge of turbulence, J. Fluid Mech. **702**, 415 (2012).
[21] C. C. T. Pringle, A. P. Willis, and R. R. Kerswell, Fully localised nonlinear energy growth optimals in pipe flow, Phys. Fluids **27**, 064102 (2015).
[22] S. M. E. Rabin, C. P. Caulfield, and R. R. Kerswell, Triggering turbulence efficiently in plane Couette flow, J. Fluid Mech. **712**, 244 (2012).
[23] S. M. E. Rabin, A variational approach to determining nonlinear optimal perturbations and minimal seeds, Ph.D. thesis, University of Cambridge, 2013.
[24] T. M. Schneider, J. F. Gibson, and J. Burke, Snakes and Ladders: Localized Solutions in Plane Couette Flow, Phys. Rev. Lett. **104**, 104501 (2010).
[25] M. Nagata, Three-dimensional finite-amplitude solutions in plane Couette flow: Bifurcation from infinity, J. Fluid Mech. **217**, 519 (1990).
[26] F. Waleffe, Homotopy of exact coherent structures in plane shear flows, Phys. Fluids. **15**, 1517 (2003).
[27] D. D. Joseph, Nonlinear stability of the Boussinesq equations by the method of energy, Arch. Ration. Mech. Anal. **22**, 163 (1966).
[28] P. Luchini and A. Bottaro, Adjoint equations for stability analysis, Annu. Rev. Fluid Mech. **46**, 493 (2014).
[29] J. R. Taylor, Numerical simulations of the stratified oceanic bottom boundary layer, Ph.D. thesis, University of California, San Diego, 2008; see also http://www.damtp.cam.ac.uk/user/jrt51/files.html for Diablo.
[30] D. Viswanath, Recurrent motions within plane Couette turbulence, J. Fluid Mech. **580**, 339 (2007).
[31] T. M. Schneider, D. Marinc, and B. Eckhardt, Localized edge states nucleate turbulence in extended plane Couette cells, J. Fluid Mech. **646**, 441 (2010).
[32] M. Salewski, J. F. Gibson, and T. M. Schneider, The origin of localized snakes-and-ladders solutions of plane Couette flow (unpublished).
[33] J. F. Gibson and E. Brand, Spanwise-localized solutions of planar shear flows, J. Fluid Mech. **745**, 25 (2014).
[34] D. Olvera and R. R. Kerswell, Exact coherent structures in stably stratifed plane Couette flow, J. Fluid Mech. (to be published).
[35] J. F. Gibson, J. Halcrow, and P. Cvitanović, Equilibrium and travelling-wave solutions of plane Couette flow, J. Fluid Mech. **638**, 243 (2009).
[36] T. S. Eaves and C. P. Caulfield, Disruption of SSP/VWI states by stable stratification, J. Fluid Mech. **784**, 548 (2015).
[37] S. Cherubini and P. De Palma, Nonlinear optimal perturbations in a Couette flow: Bursting and transition, J. Fluid Mech. **716**, 251 (2013).
[38] M. Farazmand, An adjoint-based approach for finding invariant solutions of Navier-Stokes equations, J. Fluid Mech. **795**, 278 (2016).
[39] P. G. Drazin and W. H. Reid, *Hydrodynamic Stability* (Cambridge University Press, Cambridge, 1981).
[40] R. E. Kelly, in *Physicochemical Hydrodynamics*, edited by D. B. Spaulding (Advance, London, 1977), pp. 65–79.